

Article

Analysis of Thermoacoustic Instabilities Using the Helmholtz Method in a Swirled Premixed Combustor

Zhijian Yu and Yongqing Xu *

Key Laboratory for Thermal Science and Power Engineering of Ministry of Education, Department of Energy and Power Engineering, Tsinghua University, Beijing 100084, China; zhjyu@outlook.com

* Correspondence: xuyongqing@tsinghua.edu.cn

Abstract: The Helmholtz method is developed to predict the self-excited thermoacoustic instabilities in a gas turbine combustor, combining flame describing functions, the measured damping rates under the firing condition, and the non-uniform spatial distributions of the physical parameters. The impact of the hydrodynamic and geometrical parameters on the thermoacoustic instabilities is investigated. The measured damping rates show lower values under a hot condition compared with those in a cold state. The experimental results indicate that the relative errors of the predicted eigenfrequencies and the velocity fluctuation levels are below 10%. The pressure amplitude decreases and the phase increases in the axial direction, indicating a typical 1/4-wavelength mode. At a higher equivalence ratio, the mode shape in the axial direction becomes steeper due to the elevated fluctuation amplitude at the pressure antinode after enhancing the thermal power. When the air flow rate increases, the discrepancies between the pressure shape on the flame tube side and that on the plenum side are reduced. The velocity fluctuation level increases as the combustor length increases at a constant damping rate. In fact, the velocity fluctuation level first increases and then declines, caused by more significant damping rates when employing longer flame tubes. Self-excited thermoacoustic instabilities can be well predicted using the proposed method.

Keywords: thermoacoustic instability; Helmholtz method; flame describing function; swirled premixed combustor; acoustic mode shape



Citation: Yu, Z.; Xu, Y. Analysis of Thermoacoustic Instabilities Using the Helmholtz Method in a Swirled Premixed Combustor. *Processes* **2024**, *12*, 741. <https://doi.org/10.3390/pr12040741>

Academic Editors: Hsin Chu, Ting-Ke Tseng and Birgitta Narindri Rara Winayu

Received: 19 March 2024

Revised: 1 April 2024

Accepted: 2 April 2024

Published: 5 April 2024



Copyright: © 2024 by the authors. Licensee MDPI, Basel, Switzerland. This article is an open access article distributed under the terms and conditions of the Creative Commons Attribution (CC BY) license (<https://creativecommons.org/licenses/by/4.0/>).

1. Introduction

Renewable energy has been widely employed to alleviate energy crises and carbon emissions. However, this type of energy features random volatility, high intermittency, and an uneven regional distribution. A high proportion of renewable energy power plants brings great challenges to the safety of the grid. Gas turbine power plants are excellent peak regulation apparatus due to their fast start-up and shut-down capabilities and high operational flexibilities. These properties allow the grid to accommodate more new energy resources. To meet the pollutant emission standards, the original equipment manufacturers have proposed the dry lean premixed combustion technique for gas turbines. However, serious thermoacoustic instabilities are encountered in developing this type of low-emission gas turbine combustor [1,2]. Thermoacoustic instabilities cause large-amplitude pressure fluctuations, which damage critical components of the combustor and its downstream turbine blades [3]. Meanwhile, using gas turbines to burn the hydrogen fuel produced from renewable energy is considered a nearly carbon-neutral method. The original equipment manufacturers are all developing hydrogen gas turbines to address the climate issue. For instance, the DLN 2.6e combustor for an H-class gas turbine developed by General Electric Company can burn 50% vol. H₂ at present. Hydrogen possesses a high chemical reactivity and a small Lewis number, which leads to the flame being more prone to wrinkle, and the heat release rate fluctuation is intensified. As a result, thermoacoustic instabilities become much more significant when using hydrogen fuel for carbon emission reductions [4–6], which restricts the development of hydrogen gas turbines.

Thermoacoustic instabilities are caused by interactions between heat release fluctuations and pressure fluctuations [7]. This phenomenon involves a combination of flame dynamics, combustor acoustics, burner aerodynamics, etc. [8–10]. If the thermoacoustic instabilities for a certain gas turbine combustor can be accurately numerically predicted in the design stage, the development cost and period can be significantly reduced [11]. Meanwhile, optimization of the geometric parameters can be performed based on a prediction method [12,13].

The methods for predicting thermoacoustic instabilities include the low-order network model [14–17], the Helmholtz method [18–23], and compressible large-eddy simulation [24–27]. The low-order network model is based on homogeneous acoustic elements. The acoustic wave is transmitted among the elements based on an acoustic wave equation. However, this method is available for only one- or quasi-two-dimensional structures. For real gas turbine combustors with complex three-dimensional structures, the Helmholtz solver and large-eddy simulation can be utilized to evaluate the stability of the combustion system. Large-eddy simulation needs to be combined with the time-domain impedance boundary condition [24], leading to a high computational cost. Comparatively, the Helmholtz method solved in the frequency domain has an affordable cost and seems more appropriate for industrial applications.

The Helmholtz method has been reported in many literature works. Campa et al. [28] analyzed the thermoacoustic instabilities of an annular gas turbine combustor using a three-dimensional Helmholtz method. The Helmholtz equation is discretized using the Galerkin finite element method. The corresponding growth rates, eigenfrequencies, and acoustic modes were solved using the n - τ flame transfer function. Silva et al. [19] used an in-house Helmholtz solver named AVSP to predict the limit cycle characteristics of an annular combustor. Nonlinear flame describing functions are embedded into this solver. The results indicated that the flame shape had a weak influence at low frequencies due to the small flame scale compared with the acoustic wavelength, while the opposite results were found at high frequencies. Cuquel et al. [29] compared the numerical results with experimental ones and those calculated using the low-order model. Both linear and nonlinear unstable modes, as well as the frequency and amplitude, can be obtained using the Helmholtz solver. Notably, the Helmholtz method has more potential than the low-order model when dealing with more complex geometries. Mensah et al. [30] quantified the impact of uncertainties in variables such as the equivalence ratios, geometric parameters, boundary impedance, and flame response models on the mode frequencies and growth rates of an annular combustor using an adjoint method. Non-uniform distributions of the physical parameters and the spatial flame distributions have a great influence on the predicted numerical results. Laera et al. [23] investigated the effect of the flame morphology used in the simulation on the predicted results. Conical, long cylindrical, and short cylindrical flame morphologies are compared in detail in their work. It is concluded that numerically calculated results are sensitive to flame morphologies.

The Helmholtz method has been used to numerically predict the thermoacoustic instabilities in gas turbine combustors in plentiful literature works. However, the flame response model has mainly been linear or weakly linear [31], and the physical parameters and flames have been simplified into lumped distributions. The acoustic damping rate used to determine the limit cycle is based on cold tests, which are quite different from the hot firing condition. Furthermore, the predicted results are not well compared with the experimental ones, or the prediction accuracy is unreasonable. The impact of critical operational and geometric parameters on the robustness of the numerical method has not been well explored. The corresponding physical mechanisms have not been well discussed from the numerical results.

In this work, the Helmholtz method is further developed to predict the thermoacoustic instabilities in a swirled premixed combustor. The flame describing functions are experimentally measured. The non-uniform spatial distributions of the physical parameters and flames are calculated using the CFD method and embedded into the Helmholtz solver. The damping rate for determining the limit cycle is acquired under the firing condition. The predicted results, such as the frequency, amplitude, and mode distributions, are compared in detail with the experimentally measured data. The effect of three key parameters (the equivalence ratios, air flow rates, lengths of the flame tubes) on the thermoacoustic stabili-

ties is numerically and experimentally investigated. The corresponding mechanisms are analyzed to shed light on the stability of the design of gas turbine combustors.

2. Experimental Apparatus and Procedure

2.1. Single Burner Combustor

The swirled partially premixed flame widely used in low-emission gas turbine combustors is investigated. An axial swirler with eight curved vanes is employed. There are two fuel nozzles on the pressure side and the suction side of each vane, respectively. The corresponding swirl number is 0.43. Figure 1 shows a sketch of the combustor in terms of its self-excited thermoacoustic instabilities. The experimental unit includes a plenum, an upstream section, a mixing zone, and a flame tube. The honeycomb located at the bottom of the plenum is employed to regulate the air. The premixing tube has a length of 125 mm, consisting of a swirler and a center lance. The expansion angle of the premixing outlet is 15 degrees. The flame tube has a cross-section of $160 \times 160 \text{ mm}^2$ and a length of 458.5 mm. The outlet is contracted into a small rectangular section to simulate the accelerated condition for flue gas in real gas turbines. The flame tube consists of two parts. The lower section is made of quartz glass, allowing for measuring the flame morphology and heat release rates. Under this configuration, self-excited oscillations can occur and be used to validate the numerical method for predicting thermoacoustic instabilities. Two microphones (GRAS 46BD) are mounted onto the upstream straight unit, and another two microphones (GRAS 46BL) with an interval of 150.5 mm are installed in the axial direction of the combustion chamber. The sensitivity of each microphone was preliminarily calibrated using a GRAS 42AG standard sound source. The pressure fluctuations are recorded using microphones and waveguides with a semi-infinite technique [32]. All the pressure fluctuation signals are simultaneously recorded using an acquisition card NI-9230 with a sampling rate of 12.8 kHz. Signals with a duration of 2 s are collected in each case, and the corresponding frequency resolution is 0.5 Hz. Several cases where the thermoacoustic instabilities can be observed are employed to validate the numerical prediction method.

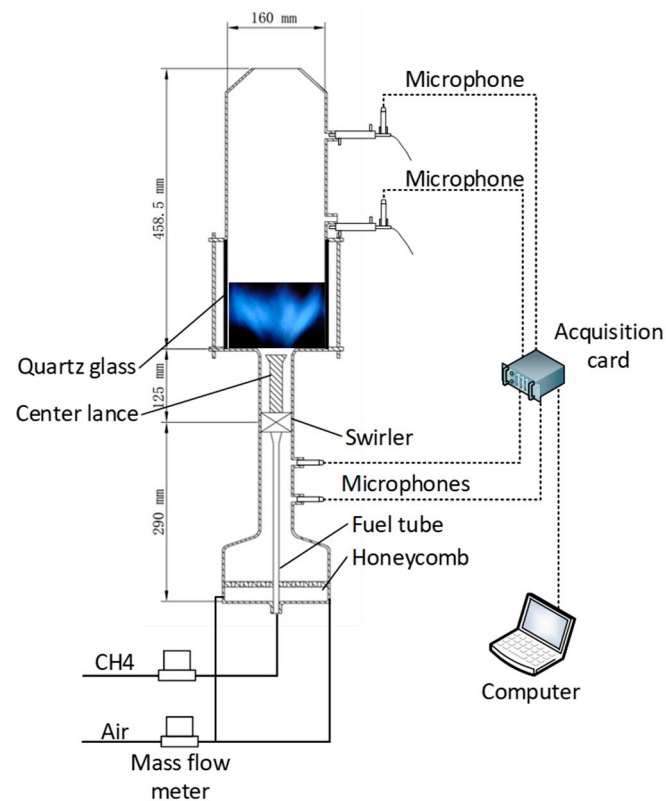


Figure 1. Sketch of the swirled partially premixed combustor.

2.2. Flame Describing Function Measurement

Two 4-inch high-sensitivity loudspeakers are mounted onto the side of the plenum as the excitation. Two 1/4-inch pressure-field microphones (GRAS 46BD) are mounted onto the side wall with an interval of 0.06 m. The velocity fluctuation level in the reference position is calculated using the two-microphone method.

The harmonic signal generated by a function generator is amplified to drive two loudspeakers. The power amplifier model is AWA 5870B, and the maximum output power is 2×150 W. The global heat release rate is measured using a CH253-type photomultiplier, manufactured by Hamamatsu Corporation. This detector is equipped with a CH* band-pass filter (430 ± 5 nm). Thus, the CH* chemiluminescence emissions, which are appropriately proportional to the heat release rate, can be converted into voltage signals [33]. Signals with a duration of 4 s are analyzed in each case, and the corresponding frequency resolution is 0.25 Hz.

The flame transfer functions can be extended to flame describing functions representing the flames' responses to different velocity fluctuation levels [34–36]. Therefore, the flame describing functions are a function of the upstream excitation frequencies and velocity fluctuation levels. The corresponding expression is listed as follows [19]:

$$\text{FDF}(\omega_r, |\hat{u}|) = G(\omega_r, |\hat{u}|) \cdot \exp(i\varphi(\omega_r, |\hat{u}|)) = \frac{\hat{Q}(\omega_r, |\hat{u}|)/\bar{Q}}{\hat{u} \cdot \mathbf{n}_{\text{ref}}/\bar{u}_{\text{ref}}} \quad (1)$$

where ω_r is the real part of the complex angular frequency, \hat{u} is the complex velocity fluctuation at the reference point, \mathbf{n}_{ref} is the reference unit vector, \hat{Q} denotes the global heat release rate fluctuation, \bar{Q} denotes the average heat release rate fluctuation, \bar{u}_{ref} is the average velocity in the reference position, and G and φ denote the gain and the phase delay.

Based on Equation (1), the flame describing function can be determined by considering the relation between the cross-correlation of the normalized velocity fluctuation level and the heat release rate fluctuation and the auto-correlation of the normalized velocity fluctuation level. The corresponding root mean square (RMS) velocity fluctuation levels $|\hat{u}_{\text{rms}}/\bar{u}|$ for testing are 0.059, 0.118, 0.236, 0.354, 0.472, and 0.590, respectively.

3. The Helmholtz Method for Predicting Thermoacoustic Instabilities

3.1. The Helmholtz Equation

Neglecting the mean flow and viscosity, the Helmholtz equation in the presence of heat release fluctuations can be simplified from Navier–Stokes equations, given as follows:

$$\frac{\lambda^2}{c^2} \hat{p} - \bar{\rho} \nabla \cdot \left(\frac{1}{\bar{\rho}} \nabla \hat{p} \right) = -\frac{\gamma - 1}{c^2} \lambda \hat{q}, \quad \lambda = -i\omega \quad (2)$$

In linear acoustics, the fluctuations can be divided into means and perturbation terms. For instance, the pressure perturbation term can be expressed as:

$$p'(\mathbf{x}) = \Re(\hat{p}(\mathbf{x}) \exp(i\omega t)) = \hat{p}(\mathbf{x}) \exp(-\omega_i t) \cos(\omega_r t) \quad (3)$$

where $\bar{(\quad)}$ denotes the mean value, (\prime) denotes the fluctuation term, $(\hat{\quad})$ denotes the complex fluctuation, γ denotes the specific heat ratio, c is the speed of sound, ρ is the air density, \Re is the real part, \mathbf{x} is the variable matrix, and $\omega = \omega_r + i\omega_i$ is the complex angular frequency. The real part $\omega_r = 2\pi f$ refers to the resonant frequency, and the imaginary part ω_i refers to the growth rate of the pressure fluctuation. A negative value of ω_i indicates the fluctuation amplitude exponentially grows with time, and a positive value results in the amplitude decaying with time. The relationship between the velocity and pressure fluctuation is given using the linearized momentum equation.

$$\nabla \hat{p} + i\omega \rho_0 \hat{u} = 0 \quad (4)$$

The combustor walls are all regarded as hard sound boundaries. The combustor outlet cannot be considered a soft sound boundary due to the radiation impedance. The corresponding radiation impedance Z_R is expressed as [37]:

$$Z_R = \frac{\hat{p}}{\hat{u}} = \overline{\rho c} \left(\frac{k_0^2 r_0^2}{4} + i0.61k_0 r_0 \right), \quad k_0 r_0 < 0.5 \quad (5)$$

where k_0 and r_0 represent the wave number and equivalence radius of the outlet, respectively. The above equations are discretized using the Galerkin finite element method. A large-scale eigenvalue equation is acquired as follows:

$$[2A]\mathbf{P} + \omega[B(\omega)]\mathbf{P} + \omega^2[C]\mathbf{P} = [D(\omega)]\mathbf{P} \quad (6)$$

Here, \mathbf{P} is the pressure eigenmode matrix, $[A]$ and $[C]$ are the discretized coefficients of the Helmholtz equation, and $[B(\omega)]$ and $[D(\omega)]$ are the discretized coefficients of the boundary conditions and the monopole acoustic source, respectively. This large-scale eigenvalue equation is solved using the commercial software COMSOL Multiphysics (Version 5.6 COMSOL). The computational domain, including the plenum, swirler, premixing tube, and combustion chamber, is modeled in detail. Unstructured tetrahedral meshes are used for the acoustic simulations, and the flame and swirler zones are refined, as shown in Figure 2. The mesh resolutions are all far smaller than $1/6$ of the minimal wavelength in the concerned frequency range of 0–600 Hz. Around 0.38 million cells are generated in each case, and the minimum cell quality is 0.19.

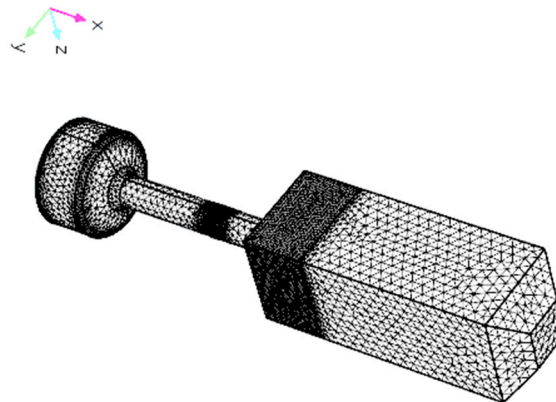


Figure 2. Non-structural mesh for the finite element method.

3.2. Distribution of the Physical Parameters and Flames

The non-uniform spatial distribution of the physical parameters and flames used for the Helmholtz solver is calculated using computational fluid dynamic simulations. The local heat release fluctuation \hat{q} inside the flame region is introduced as:

$$\hat{q} = \left(\frac{\text{PFR}(\mathbf{x})}{\text{PFR}_{\text{total}}} \cdot \overline{Q} \right) \cdot \frac{\hat{u}}{\bar{u}} \text{FDF}(\omega_r, |\hat{u}|) \quad (7)$$

where $\text{PFR}(\mathbf{x})$ is the local product formation rate in the flame region, $\text{PFR}_{\text{total}}$ is the volume integral of the product formation rates, and \overline{Q} is the total thermal power. The physical parameter fields calculated using the CFD simulation need to be imported into the finite element mesh in COMSOL. These fields include the temperature, density, sound velocity, and flame heat release rate. The k- ω SST turbulence model is selected for the simulation. A partially premixed combustion model and the GRI-Mech 3.0 reaction mechanism are employed. The gas density is determined using the incompressible ideal gas state equation, and the kinetic viscosity is modeled using the Sutherland model. A mass inlet boundary condition is employed for the air and fuel inlets, while a pressure outlet boundary is used

for the outlet. An axial linearly distributed temperature is used for the flame tube wall. The control equations are iteratively solved using the SIMPLE algorithm. Parameters such as the pressure, momentum, and turbulent kinetic energy are discretized using the second-order scheme. Figure 3 shows the velocity distributions at $x = 0.155$ mm for 1.9, 2.8, and 4.0 million grids, respectively. The change in the velocity fields is not obvious when the grid quantity increases from 2.8 million to 4.0 million. Therefore, 2.8 million cells are selected for the RANS calculations.

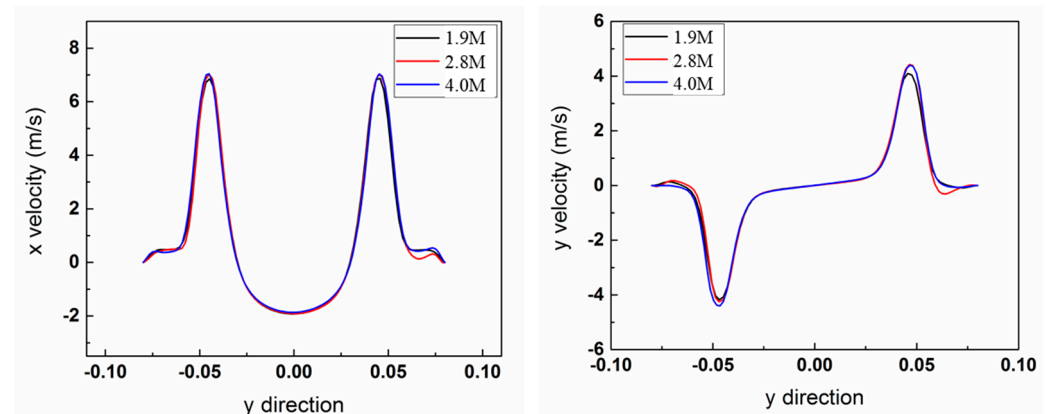


Figure 3. Grid independence analysis.

Figure 4 illustrates comparisons of the temperature and heat release rate fields before and after importing the CFD results into the finite element mesh. The pattern of each parameter remains consistent before and after the import procedure. Both heat release rate distributions exhibit a V-shaped structure, anchored in the same position at the burner exit. The total product formation rates are 0.0375 m^3/s and 0.0378 m^3/s before and after importing, respectively, with a relative error of 0.8%.

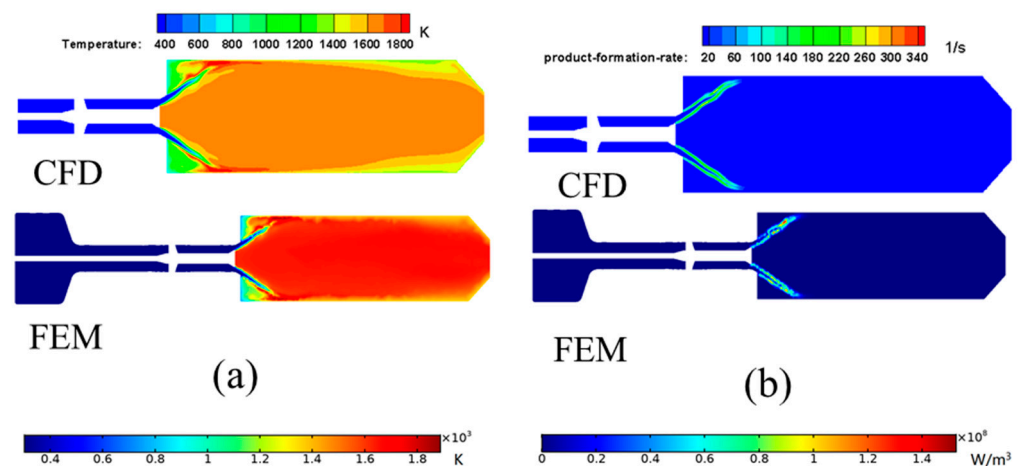


Figure 4. Comparison of raw and interpolated distributions of physical parameters. (a) Temperature and (b) flame heat release rate.

4. Results and Discussion

4.1. Measured Damping Rate

It is considered that the limit cycle state is reached when the numerically calculated growth rate equals the damping rate of the combustion system. In this paper, the damping rate is acquired using experimental frequency response tests. The damping rate is then estimated by analyzing the sharpness of the response curve.

The response curve under the cold condition shows a peak frequency of 455 Hz, which equals the first-order eigenfrequency of the combustion system in the cold state. When the

air flow rate increases to 500 L/min, the damping rate under the cold condition decreases from 20.4 rad/s to 17.0 rad/s. This is due to the increasing air flow rate, which reduces the streamwise propagation resistance of an acoustic wave.

The previous results were mainly obtained under cold conditions and are quite different from those under hot conditions.

Figure 5 presents a comparison of the measured damping rates under the hot firing condition for different operating conditions. The response frequency peak is located at approximately 80 Hz under the hot condition. This frequency equals the first-order eigenfrequency of the combustion system in the hot state. The frequency response curve has additional noise caused by combustion, while the primary peak can still be distinctly identified. The measured damping rate for each condition ranges from 4.7 to 11.3 rad/s under the hot condition. The measured damping rate increases with an increase in the air flow rates. This is likely due to the higher thermal power and temperature in the combustion chamber at a higher air flow rate, which increases the dynamic viscosity and leads to a greater damping dissipation.

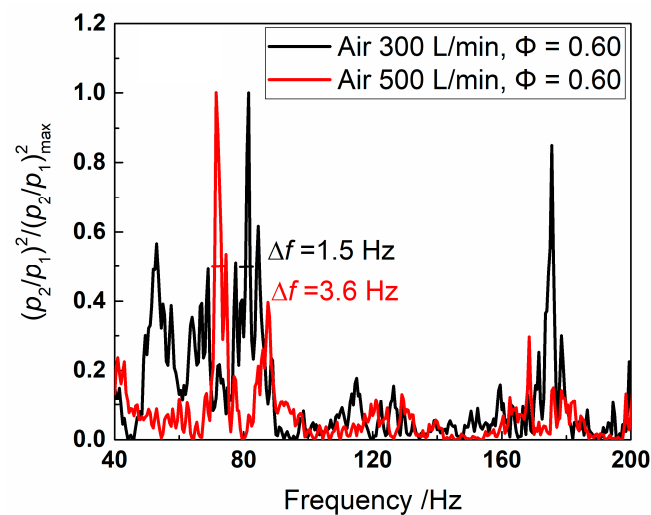


Figure 5. Comparison of measured damping rates under the hot firing condition.

4.2. Interpolated Flame Describing Functions

The Helmholtz method for predicting thermoacoustic instabilities requires continuous flame describing function data, while the experimentally measured results are discrete points. Therefore, the gains and phases of the measured flame describing functions are first interpolated before being imported into the Helmholtz solver. Spline interpolations are used for data in the velocity fluctuation range of 0.059~0.59. Then, the measured data at other velocity fluctuation amplitudes are derived using linear interpolations and extrapolations. The phase results are all interpolated using a linear method. Figure 6 displays the interpolated flame describing functions of typical cases for numerical simulations, and black dots represent the experimentally measured results. As shown in Figure 6, the gains of the flame describing functions display a bimodal distribution, whose peak frequencies are located between 50–100 Hz and 100–200 Hz, respectively. The peak values of the gains decline with an increase in the velocity fluctuation levels, indicating the nonlinear saturation of swirling flames [34]. The phase curves are basically proportional to the frequency, which means a constant time delay between the velocity fluctuations and heat release rate fluctuations. Singularities and misplaced values are not observed in the interpolated results. The interpolated flame describing functions can be efficiently used for the Helmholtz method.

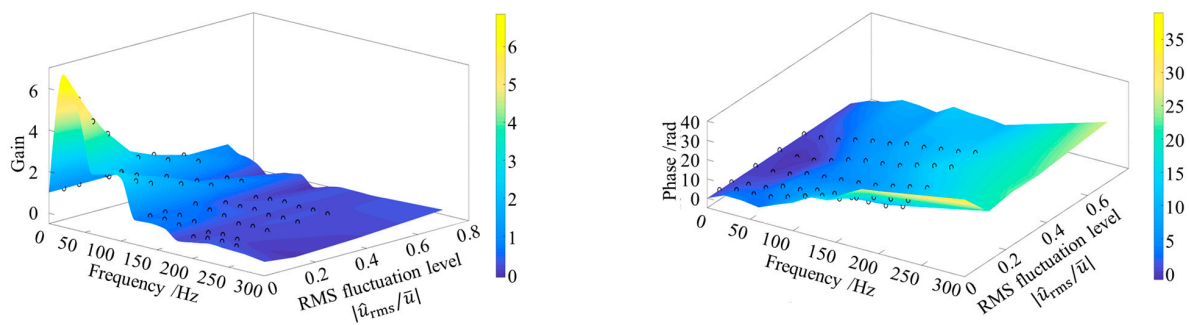


Figure 6. Interpolated flame describing function of typical cases for numerical simulations at an air flow rate of 500 L/min and an equivalence ratio of 0.65. (black dots represent experimentally measured results. Left: gain; right: phase).

4.3. Effect of Equivalence Ratios

The numerically predicted eigenfrequencies, velocity fluctuation levels, and mode shapes at the limit cycle of the thermoacoustic instabilities for different equivalence ratios are compared with the experimentally measured ones. The air volume flow rate is 500 L/min in this section, and the respective equivalence ratios are 0.55, 0.65, and 0.68. When the equivalence ratio is 0.55, thermoacoustic instabilities are not observed at this air flow rate. The measured damping rates under the firing condition are 11.3, 10.8, and 10.8 rad/s for the above equivalence ratios, respectively.

The trajectories of the numerically calculated growth rates of the first-order mode, along with the velocity fluctuation levels for different equivalence ratios, are shown in Figure 7. The calculated growth rates are all smaller than the measured damping rates when the velocity fluctuation level is beyond 0.6 at an equivalence ratio of 0.55. The thermoacoustic oscillations in the combustor will be dissipated so that the limit cycle state is not approached, which is consistent with the fact that thermoacoustic instabilities are not observed during the experiment under this operation condition. When the equivalence ratios are 0.65 and 0.68, the numerically calculated growth rates decline from positive values across the damping rate band to negative ones and rebound after reaching the lowest values. The calculated growth rates tend to be constant at higher velocity fluctuation levels. The limit cycle state is reached when the growth rate is equal to the damping rate. Specifically, when the velocity fluctuation is greater than a certain value, the growth rate increases, which is different from the previous trend. This is due to the fact that there are two adjacent gain peaks. With an increase in the velocity fluctuation levels, the calculated frequency reduces, and the frequency points shift from the band-pass peak to the low-pass one, causing a raising growth rate. Finally, the frequency moves to the valley of the gain curves, reaching an equilibrium state.

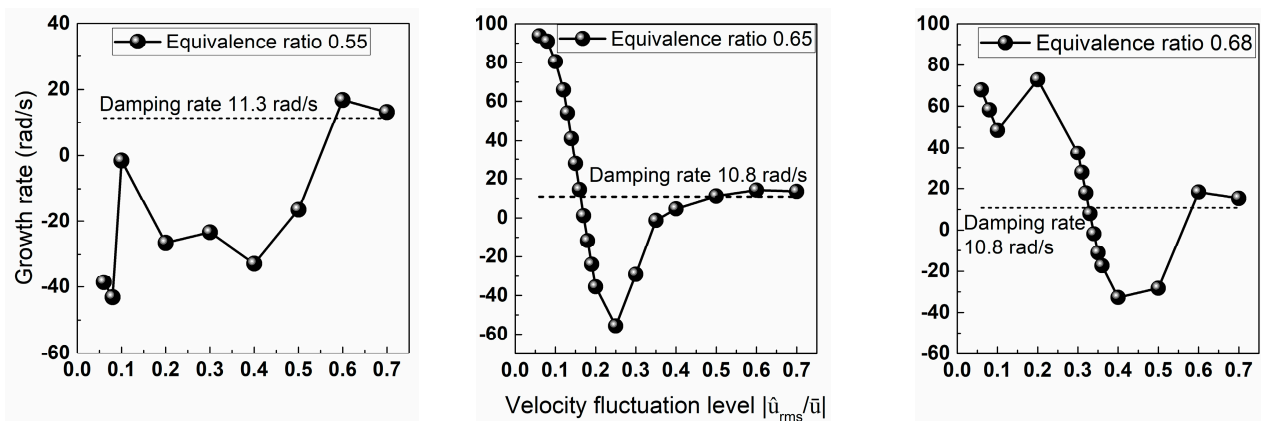


Figure 7. Evolution of calculated growth rates of the first-order mode along with the velocity fluctuation levels for different equivalence ratios at an air volume flow rate of 500 L/min.

The trajectories of the simulated growth rates of the second-order mode, along with the velocity fluctuation levels for different equivalence ratios, are shown in Figure 8. For the above equivalence ratios, with an increase in the velocity fluctuation levels, the numerically calculated growth rates increase from negative values across the damping rate band to positive ones and decline to negative values after reaching the maximum. Notably, instability is triggered by initial tiny external perturbations. These perturbations are at a low level in the initial phase. Thus, the growth rate is negative, as presented in Figure 8, which indicates the initial oscillation will be dissipated and the limit cycle cannot be reached. Therefore, the second-order mode is attenuated by dissipations, which is consistent with the result that second-order pressure oscillations are not observed during the experiments.

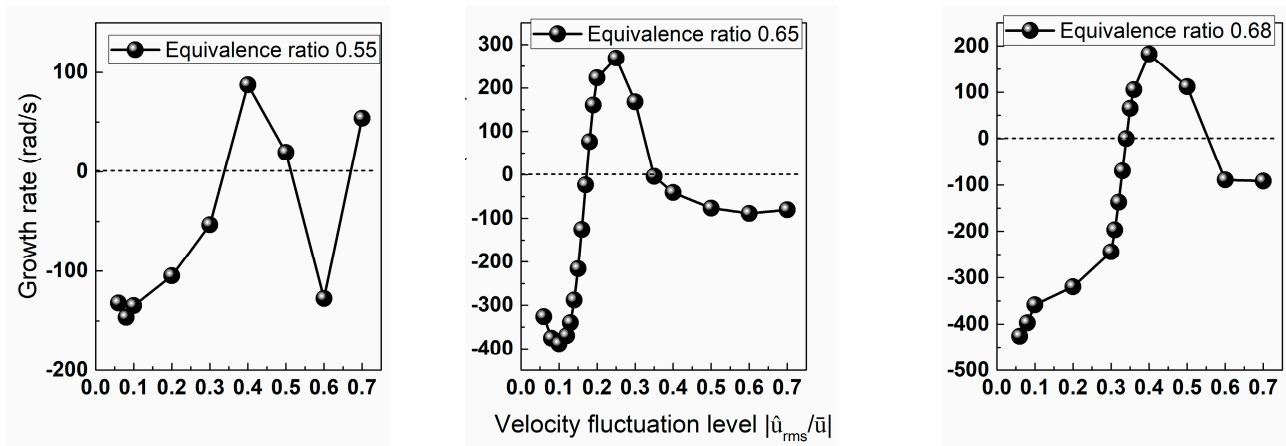


Figure 8. Evolution of calculated growth rates of the second-order mode along with the velocity fluctuation levels for different equivalence ratios at an air volume flow rate of 500 L/min.

Table 1 displays a comparison of the eigenfrequencies and RMS velocity fluctuation levels at the limit cycle for the experimentally measured data and numerically predicted results under different equivalence ratios. Each case is performed three times to eliminate accidental errors. When the equivalence ratio is 0.55, the numerically calculated growth rate trajectories demonstrate that self-excited instabilities cannot be formed, in accordance with the experimental results. At an equivalence ratio of 0.65, the experimentally measured and numerically predicted eigenfrequencies are 81.7 Hz and 73.4 Hz, respectively, obtaining an absolute error of 8.3 Hz. The corresponding experimentally measured and numerically predicted velocity fluctuation levels are 0.19 and 0.16, and the absolute error is 0.03. At an equivalence ratio of 0.68, the absolute errors of the predicted eigenfrequency and velocity fluctuation level are 7.4 Hz and 0.10. The minimum relative errors of the predicted frequencies are all within 10%, and the absolute errors of the predicted velocity fluctuation levels are in the range of 0.007–0.08, which indicates this prediction method has a satisfactory precision. Meanwhile, the trend in the variation in the predicted results, along with the equivalence ratio, is consistent with that of the experimental ones. While previous literature works [18] have mostly used the linear method, which can only predict eigenfrequencies, this paper successfully predicts both the eigenfrequencies and amplitudes of self-excited oscillations. Compared with research works [19,22], using the non-linear model, the prediction errors for the eigenfrequencies and amplitudes have been reduced from 20% to around 10% in this work.

As the predicted results are in good agreement with the experimental ones, the mode shape of the pressure fluctuation in the combustor can be further analyzed based on the numerical results. Figure 9 presents the axial pressure distributions of the first-order modes for two equivalence ratios. The pressure amplitude decreases in the axial direction. With respect to the first-order mode, the pressure shape maintains the highest value on the plenum side and the lowest value at the exit of the combustion chamber, indicating that the pressure shape is dominated by the cold section. For the second-order mode, the

pressure pulsation maintains the highest value in the flame region and decreases at the two ends, indicating that the mode shape is dominated by the flames. The pressure amplitude distribution in the combustor is a superposition of all the order modes. As the growth rate of the second-order mode is negative, the first-order mode shape can be regarded as the actual pressure fluctuation distribution in the combustor. The numerical results indicate the pressure amplitude has the highest value on the plenum side. The experimentally measured results show that the pressure fluctuation amplitude on the plenum side is almost 300 Pa and that on the combustion chamber side it is around 100 Pa. This pressure mode distribution from the experiments is consistent with the numerically predicted one.

Table 1. Comparison of eigenfrequencies and RMS velocity fluctuation levels at the limit cycle for experimentally measured data and numerically predicted ones under different equivalence ratios at an air volume flow rate of 500 L/min.

Equivalence Ratio	Frequency/Hz		Velocity Fluctuation Level	
	Exp.	Num.	Exp.	Num.
$\Phi = 0.55$	Not self-excited	Not self-excited	Not self-excited	Not self-excited
$\Phi = 0.65$	81.7	73.4	0.19	0.16
$\Phi = 0.68$	83.0	75.6	0.23	0.33

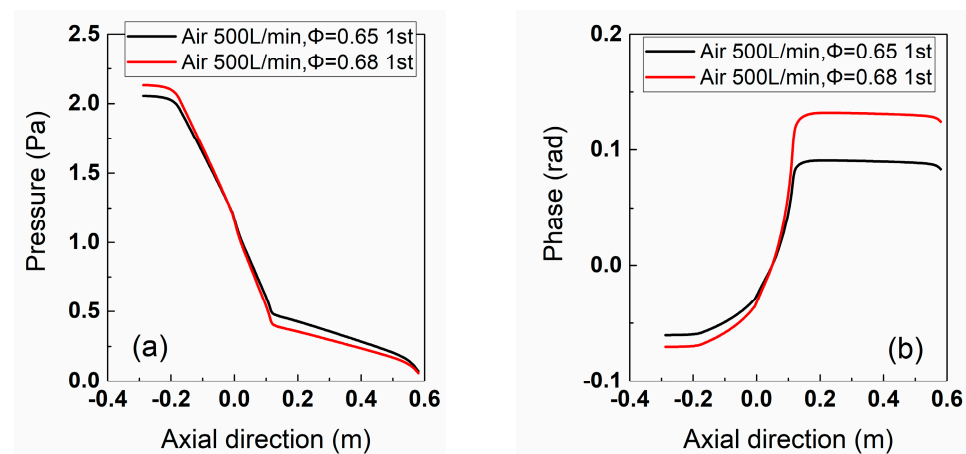


Figure 9. Pressure shape of the first-order mode in the axial direction for different equivalence ratios. (a) Pressure and (b) phase.

In the plenum, the pressure amplitude rapidly declines, while it decreases more gradually in the combustion chamber. This is due to the small diameter of the premixing tube, which suddenly expands to a larger cross-section of the flame tube. The pressure pulsation at the exit of the combustion chamber is not zero because of the radiation impedance, which causes the node of the pressure fluctuations to shift. It is observed that the pressure amplitude at the antinode is elevated at a higher equivalence ratio. This is due to the larger thermal power at a higher equivalence ratio, which leads to more significant pressure pulsations than the combustion system can maintain. As a result, the pressure amplitude is elevated at the antinode. The phase of the pressure fluctuations differs between the flame tube side and the plenum side. This means that when the pressure fluctuation increases on the flame tube side, it decreases on the plenum side.

4.4. Effects of Air Flow Rates

From the preliminary experiments, thermoacoustic instabilities only occur when the Reynolds number reaches a certain value. Therefore, it is necessary to further investigate whether the numerical method can efficiently predict the thermoacoustic instability properties at different air flow rates. A comparison of the numerically calculated and experimentally measured results is carried out at air flow rates of 300 L/min and 400 L/min

with an equivalent ratio of 0.7, respectively. The experimental results indicate that thermoacoustic oscillations are not observed for all the equivalence ratios at an air flow rate of 300 L/min. When the air flow rate is 400 L/min, the oscillations present a limit cycle feature at an equivalence ratio of 0.70.

Figures 9 and 10 depict the trajectories of the calculated growth rates and eigenfrequencies of the first- and second-order modes, along with the velocity fluctuation levels, at air volume flow rates of 300 and 400 L/min and an equivalence ratio of 0.7. At an air flow rate of 300 L/min and an equivalence ratio of 0.7, the growth rates of the first- and second-order modes increase from negative values to positive ones and subsequently oscillate around the damping rate. At the initial stage, the amplitude of the fluctuations is weak and the growth rate is less than the damping rate, which indicates the initial external perturbation will be dissipated and cannot further develop into the limit cycle. This result is consistent with the experimental phenomenon that no thermoacoustic oscillations are observed at this air flow rate.

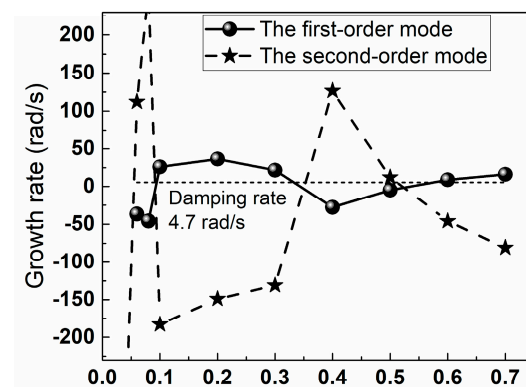


Figure 10. Evolution of calculated growth rates of the first- and second-order modes, along with the velocity fluctuation levels, at an air volume flow rate of 300 L/min and an equivalence ratio of 0.7.

At an air flow rate of 400 L/min and an equivalence ratio of 0.7, with an increase in the velocity fluctuation level, the numerically calculated growth rate declines from a positive value to a negative one and gradually increases after reaching the critical position, remaining at a value below the damping rate. At this equivalence ratio, pressure fluctuations can develop from the initial tiny perturbations in the limit cycle oscillation, which were detected during the self-excited experiment. Under this operating condition, the growth rate of the second-order mode changes from a negative value to a positive one, which means the second-order mode is difficult to trigger. (See Figure 11).

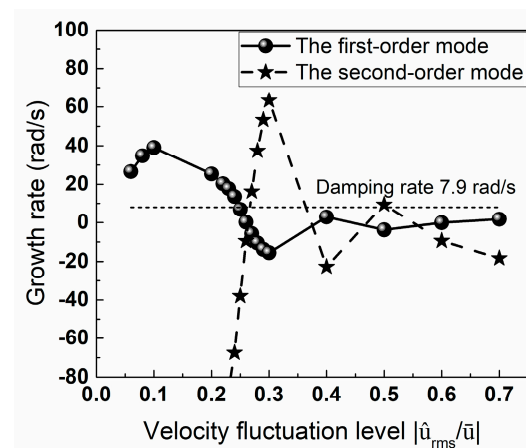


Figure 11. Evolution of calculated growth rates of the first- and second-order modes, along with the velocity fluctuation levels, at an air volume flow rate of 400 L/min and an equivalence ratio of 0.7.

Table 2 presents a comparison of the eigenfrequencies and RMS velocity fluctuation levels at the limit cycle for the experimentally measured data and numerically predicted results under different air flow rates. The numerical method can successfully predict whether thermoacoustic instabilities could occur. In the self-excited case, the absolute errors of the predicted eigenfrequencies and velocity fluctuation levels are 8.8 Hz and 0.03, respectively. Combining the flame describing functions, the measured damping rates under the firing condition, and the non-uniform distributions of the physical parameters and flames, whether self-excited thermo-acoustic instabilities occur and the corresponding parameters can be well predicted using the Helmholtz method.

Table 2. Comparison of eigenfrequencies and RMS velocity fluctuation levels at the limit cycle for experimentally measured data and numerically predicted ones under different air flow rates.

Case	Frequency/Hz		Velocity Fluctuation Level	
	Exp.	Num.	Exp.	Num.
Air 300 L/min, $\Phi = 0.70$	/	/	/	/
Air 400 L/min, $\Phi = 0.70$	77.5	86.3	0.28	0.25

Figure 12 displays the pressure shape of the first-order mode in the axial direction for different air flow rates. It can be observed that the pressure amplitude of the first-order mode on the plenum side is larger than that on the combustion chamber side. The pressure shape distinctly shows a 1/4-wavelength mode. On the plenum side, the pressure pulsation at an air flow rate of 400 L/min is higher than that at 500 L/min. On the combustion chamber side, the pressure pulsation is lower at 400 L/min. The thermal power maintains a lower value at a lower relative air flow rate, resulting in a decreasing pressure pulsation energy. The axial distribution of the phase in the plenum is similar under these two conditions. However, the phase value on the combustion chamber side at an air flow rate of 400 L/min is significantly larger than that at 500 L/min. This discrepancy may be caused by the varying levels of flame–acoustic interactions between the two conditions. The pressure pulsation on the combustion chamber side varies more significant than that on the plenum side. The proposed numerical prediction method can efficiently capture the changes in the mode shapes at various air flow rates and with different flame morphologies.

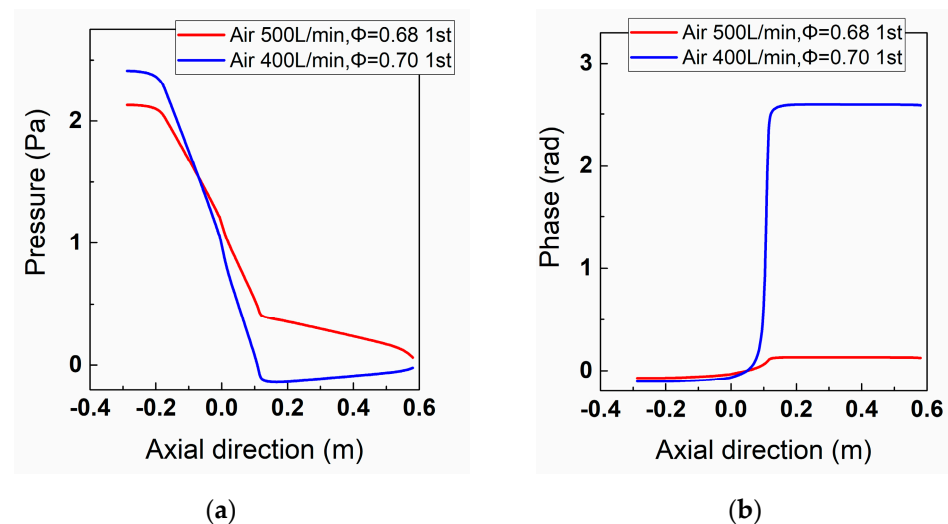


Figure 12. Pressure shape of the first-order mode in the axial direction for different air flow rates. (a) Pressure and (b) phase.

4.5. Effect of the Length of the Combustor

If the length of the combustor is sufficient for a combustion reaction, there is a minimal impact of the length on the flame morphology. However, the thermoacoustic instability characteristics are affected by the flame pattern, which may be altered by the flame tube length. In this work, the shortest flame tube length was selected to be larger than 200 mm in order to avoid the impact of the flame tube length on the flame morphology.

Figure 13 displays the evolution of the calculated growth rates and frequencies of the first-order modes, along with the velocity fluctuation levels, for different flame tube lengths. For the first-order mode, the growth rate maintains a higher initial value at a larger flame tube length. Additionally, the growth rate decreases more rapidly with an increase in the velocity fluctuation level. Conversely, for a shorter flame tube, the initial value of the growth rate is smaller, and the growth rate gradually declines as the velocity fluctuation level increases. The effect of the flames, serving as a sound source, on the thermoacoustic instabilities becomes more profound at a larger flame tube length since the flame is far away from the exit. Figure 13 also shows that the frequency of the first-order mode shifts downwards as the length of the flame tube increases. The acoustic wavelength in the combustor increases with an increase in the flame tube length, resulting in a lower eigenfrequency value when the speed of sound is constant.

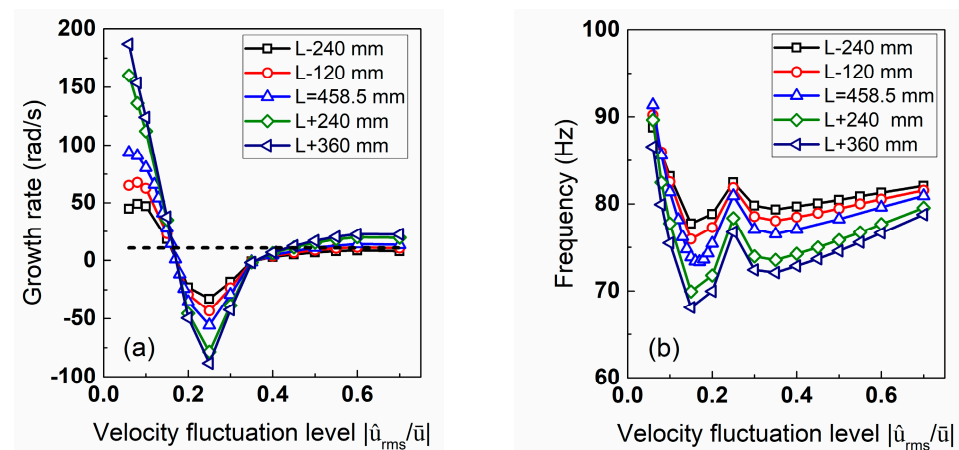


Figure 13. Evolution of calculated growth rates and frequencies of the first-order modes, along with the velocity fluctuation levels, for different flame tube lengths. (a) Growth rate and (b) frequency.

Assuming that the effect of the flame tube length on the damping rates can be neglected, the numerically calculated velocity fluctuation levels and the eigenfrequencies for different flame tube lengths are shown in Figure 14. As the flame tube length increases, the velocity fluctuation level at the limit cycle increases due to the fact that the reference point is further away from the exit of the combustion chamber, which is the node of the acoustic wave. The flame serving as an acoustic source is more favorable for the pulsation when it is further away from the wave node. However, in a real situation, the longer the flame tube length, the greater the acoustic damping rate of the combustion system; thus, the velocity fluctuation level decreases. It can be asserted that thermoacoustic instabilities are unlikely to occur when the combustion chamber length is short since the growth rate is not large enough at a short flame tube length. Under a real condition, the fluctuation level of the thermoacoustic instabilities will first increase and then decrease with an increase in the flame tube length because of the increasing damping rate caused by the longer flame tube. Eventually, the thermoacoustic instabilities will be suppressed when the flame tube reaches a certain length.

Previous studies [21] have reported that thermoacoustic instabilities can only occur within a specific flame tube length range. Both excessively long and short flame tubes are unlikely to trigger thermoacoustic instabilities. The numerically predicted results are consistent with the experimental ones. The numerical results indicate that the eigenfre-

quencies decline as the length of the flame tube increases. In this combustor, which shows a $1/4$ -wavelength pressure mode, the acoustic wavelength increases as the flame tube length increases. According to the frequency formula, at the constant speed of sound, a longer flame tube may cause higher-eigenfrequency pressure fluctuations.

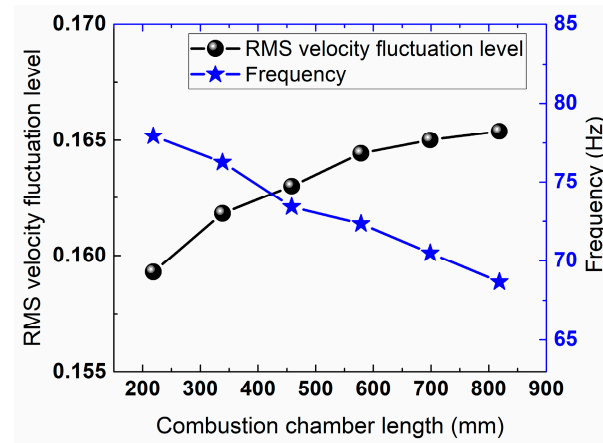


Figure 14. Velocity fluctuation levels and eigenfrequencies for different flame tube lengths.

The impact of the flame tube length on the mode distributions of the first-order modes is further analyzed. Figure 15 shows the corresponding impact on the axial pressure distribution of the first-order modes. It is evident that a shorter flame tube results in a shorter $1/4$ -wavelength distribution, leading to a higher amplitude at the pressure antinode. Conversely, a longer flame tube results in a more gradual $1/4$ -wavelength distribution.

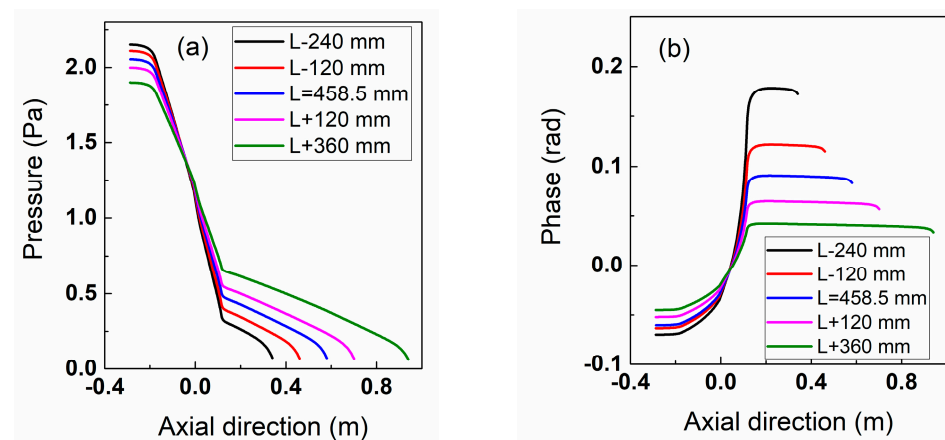


Figure 15. Pressure shape of the first-order mode in the axial direction for different flame tube lengths. (a) Pressure and (b) phase.

As the length of the flame tube increases, the flame, serving as a sound source, is necessary to drive more fluid particles. Therefore, each fluid particle is allocated less kinetic energy, resulting in weaker pressure fluctuations. Additionally, as the flame tube length increases, the value of the phases in the flame tube decreases. The results indicate that the difference between the pressure on the flame tube side and that on the plenum side is reduced.

5. Conclusions

The Helmholtz method, combining the measured flame describing functions, the measured damping rates under the hot condition, and the non-uniform spatial distribution of the physical parameters, is developed to predict the self-excited thermoacoustic oscillation in a swirled premixed gas turbine combustor. The predicted results are compared in

detail with the experimental ones. The acoustic damping rates under the hot condition are compared with those in the cold state. The effect of the equivalence ratios, air flow rates, and flame tube lengths on the thermoacoustic instabilities is investigated.

The response curve of the damping rate exhibits a peak frequency near 455 Hz under the cold condition, while the peak frequency shifts to around 80 Hz under the firing condition. The damping rates decline in thermal states due to the flames' amplification of the propagation of the acoustic waves.

The eigenfrequencies, fluctuation levels, and pressure mode shapes of the self-excited thermoacoustic instabilities at various equivalence ratios and air flow rates can be accurately calculated using the developed Helmholtz method. The predicted eigenfrequencies and fluctuation levels have relative errors of less than 10%. The predicted results indicate that the pressure amplitude decreases in the axial direction. At a higher equivalence ratio, the mode shape in the axial direction becomes steeper due to the increased pulsation energy after enhancing the thermal power. The pressure fluctuation level at the antinode is accordingly enhanced. Regarding the phase, as the air flow rate increases, the axial distribution of the phase on the plenum side remains unchanged, while that on the combustion chamber side decreases, caused by the acoustic transmission characteristics across flames.

The velocity fluctuation level increases as the length of the flame tube increases at a constant damping rate. In fact, when the length of the flame tube increases, the damping rates accordingly increase, resulting in the fact that the fluctuation levels first increase and then decrease. Additionally, the eigenfrequency decreases as the flame tube length increases. The axial pressure shape becomes smoother for a longer flame tube because more fluid particles need to be mobilized. As the flame tube length increases, the difference between the pressure on the flame tube side and that on the plenum side is reduced.

The proposed prediction scheme for thermoacoustic instabilities can be effectively utilized to evaluate the stability of combustors in the design stage, resulting in decreased experimental costs. The corresponding geometrical parameters can be optimized based on a numerical prediction method. Additionally, the predicted results can be employed to determine the optimal parameters and installation locations for external thermoacoustic suppression devices.

Author Contributions: Conceptualization, Z.Y. and Y.X.; methodology, Z.Y.; validation, Z.Y.; formal analysis, Z.Y.; investigation, Z.Y.; data curation, Z.Y.; writing—original draft preparation, Z.Y.; writing—review and editing, Y.X.; visualization, Y.X.; supervision, Y.X.; project administration, Z.Y.; funding acquisition, Y.X. All authors have read and agreed to the published version of the manuscript.

Funding: This research was funded by the National Natural Science Foundation of China, grant number 52206147.

Data Availability Statement: Data are contained within the article.

Conflicts of Interest: The authors declare no conflicts of interest.

References

1. Lieuwen, T.; Yang, V. *Combustion Instabilities in Gas Turbines: Operational Experience, Fundamental Mechanisms, and Modeling*; AIAA: Reston, VA, USA, 2005; pp. 284–285.
2. O'Connor, J. Understanding the role of flow dynamics in thermoacoustic combustion instability. *Proc. Combust. Inst.* **2023**, *39*, 4583–4610. [[CrossRef](#)]
3. Rywik, M.; Kasthuri, P.; Boxx, I.; Chterev, I.; Polifke, W.; Sujith, R.I. Turbulence and heat release rate network structure in hydrogen-enriched combustion. *Proc. Combust. Inst.* **2023**, *39*, 4701–4710. [[CrossRef](#)]
4. Lee, T.; Kim, K.T. Direct comparison of self-excited instabilities in mesoscale multinozzle flames and conventional large-scale swirl-stabilized flames. *Proc. Combust. Inst.* **2021**, *38*, 6005–6013. [[CrossRef](#)]
5. Noble, D.; Wu, D.; Emerson, B.; Sheppard, S.; Lieuwen, T.; Angello, L. Assessment of current capabilities and near-term availability of hydrogen-fired gas turbines considering a low-carbon future. *J. Eng. Gas Turbines Power* **2021**, *143*, 041002. [[CrossRef](#)]
6. Kang, H.; Lee, T.; Jin, U.; Kim, K.T. Experimental investigation of combustion instabilities of a mesoscale multinozzle array in a lean-premixed combustor. *Proc. Combust. Inst.* **2021**, *38*, 6035–6042. [[CrossRef](#)]

7. Schuermans, B.; Moeck, J.; Blondé, A.; Dharmaputra, B.; Noiray, N. The Rayleigh integral is always positive in steadily operated combustors. *Proc. Combust. Inst.* **2023**, *39*, 4661–4669. [[CrossRef](#)]
8. Kwak, S.; Choi, J.; Lee, M.C.; Yoon, Y. Attenuation of combustion instability in a fuel-staged dual-nozzle gas turbine combustor with asymmetric hydrogen composition. *Proc. Combust. Inst.* **2023**, *39*, 4681–4690. [[CrossRef](#)]
9. Karmarkar, A.; Gupta, S.; Boxx, I.; Hemchandra, S.; O'Connor, J. Impact of precessing vortex core dynamics on the thermoacoustic instabilities in a swirl-stabilized combustor. *J. Fluid Mech.* **2022**, *946*, A36. [[CrossRef](#)]
10. Vignat, G.; Durox, D.; Renaud, A.; Lancien, T.; Vicquelin, R.; Candel, S. Investigation of transient PVC dynamics in a strongly swirled spray flame using high speed planar laser imaging of SnO₂ microparticles. *Combust. Flame* **2021**, *225*, 305–319. [[CrossRef](#)]
11. Poinot, T. Prediction and control of combustion instabilities in real engines. *Proc. Combust. Inst.* **2017**, *36*, 1–28. [[CrossRef](#)]
12. Mensah, G.A.; Moeck, J.P. Acoustic damper placement and tuning for annular combustors: An adjoint-based optimization study. *J. Eng. Gas Turbines Power* **2017**, *139*, 061501. [[CrossRef](#)]
13. Pérez, J.G.A. Sensitivity Analysis and Optimization in Low Order Thermoacoustic Models. Ph.D. Thesis, University of Cambridge, Cambridge, UK, 2019.
14. Bauerheim, M.; Parmentier, J.-F.; Salas, P.; Nicoud, F.; Poinot, T. An analytical model for azimuthal thermoacoustic modes in an annular chamber fed by an annular plenum. *Combust. Flame* **2014**, *161*, 1374–1389. [[CrossRef](#)]
15. Magri, L.; Bauerheim, M.; Juniper, M.P. Stability analysis of thermo-acoustic nonlinear eigenproblems in annular combustors. Part I. Sensitivity. *J. Comput. Phys.* **2016**, *325*, 395–410. [[CrossRef](#)]
16. Kruger, U.; Wren, J.; Hoffmann, S.; Krebs, W. Prediction of Thermoacoustic Instabilities with Focus on the Dynamic. In Proceedings of the International Gas Turbine and Aeroengine Congress and Exhibition, Indianapolis, IN, USA, 7–10 June 1999.
17. Moeck, J.P.; Durox, D.; Schuller, T.; Candel, S. Nonlinear thermoacoustic mode synchronization in annular combustors. *Proc. Combust. Inst.* **2019**, *37*, 5343–5350. [[CrossRef](#)]
18. Camporeale, S.M. A finite element method for three-dimensional analysis of thermo-acoustic combustion instability. *J. Eng. Gas Turbines Power* **2011**, *133*, 011506. [[CrossRef](#)]
19. Silva, C.F.; Nicoud, F.; Schuller, T.; Durox, D.; Candel, S. Combining a Helmholtz solver with the flame describing function to assess combustion instability in a premixed swirled combustor. *Combust. Flame* **2013**, *160*, 1743–1754. [[CrossRef](#)]
20. Campa, G.; Camporeale, S.M. Prediction of the thermoacoustic combustion instabilities in practical annular combustors. *J. Eng. Gas Turbines Power* **2014**, *136*, 091504. [[CrossRef](#)]
21. Kim, S.-K.; Kim, D.; Cha, D.J. Finite element analysis of self-excited instabilities in a lean premixed gas turbine combustor. *Int. J. Heat Mass Transfer* **2018**, *120*, 350–360. [[CrossRef](#)]
22. Laera, D.; Camporeale, S.M. A weakly nonlinear approach based on a distributed flame describing function to study the combustion dynamics of a full-scale lean-premixed swirled burner. *J. Eng. Gas Turbines Power* **2017**, *139*, 091501. [[CrossRef](#)]
23. Laera, D.; Prieur, K.; Durox, D.; Schuller, T.; Camporeale, S.M.; Candel, S. Impact of heat release distribution on the spinning modes of an annular combustor with multiple matrix burners. *J. Eng. Gas Turbines Power* **2017**, *139*, 051505. [[CrossRef](#)]
24. Wolf, P.; Staffelbach, G.; Gicquel, L.Y.M.; Müller, J.-D.; Poinot, T. Acoustic and Large Eddy Simulation studies of azimuthal modes in annular combustion chambers. *Combust. Flame* **2012**, *159*, 3398–3413. [[CrossRef](#)]
25. Franzelli, B.; Riber, E.; Gicquel, L.Y.M.; Poinot, T. Large Eddy Simulation of combustion instabilities in a lean partially premixed swirled flame. *Combust. Flame* **2012**, *159*, 621–637. [[CrossRef](#)]
26. Schulz, O.; Doll, U.; Ebi, D.; Droujko, J.; Bourquard, C.; Noiray, N. Thermoacoustic instability in a sequential combustor: Large eddy simulation and experiments. *Proc. Combust. Inst.* **2019**, *37*, 5325–5332. [[CrossRef](#)]
27. Chen, Z.X.; Langella, I.; Swaminathan, N.; Stöhr, M.; Meier, W.; Kolla, H. Large Eddy Simulation of a dual swirl gas turbine combustor: Flame/flow structures and stabilisation under thermoacoustically stable and unstable conditions. *Combust. Flame* **2019**, *203*, 279–300. [[CrossRef](#)]
28. Campa, G.; Camporeale, S.M. Influence of Flame and Burner Transfer Matrix on Thermoacoustic Combustion Instability Modes and Frequencies. In Proceedings of the ASME Turbo Expo 2010: Power for Land, Sea and Air, Scotland, UK, 14–18 June 2010.
29. Cuquel, A.; Silva, C.; Nicoud, F.; Durox, D.; Schuller, T. Prediction of the Nonlinear Dynamic of a Multiple Flame. In Proceedings of the ASME Turbo Expo 2013: Turbine Technical Conference and Exposition, San Antonio, TX, USA, 3–7 June 2013.
30. Mensah, G.A.; Magri, L.; Orchini, A.; Moeck, J.P. Effects of asymmetry on thermoacoustic modes in annular combustors: A higher-order perturbation study. *J. Eng. Gas Turbines Power* **2019**, *141*, 041030. [[CrossRef](#)]
31. Polifke, W. Modeling and analysis of premixed flame dynamics by means of distributed time delays. *Prog. Energy Combust. Sci.* **2020**, *79*, 100845. [[CrossRef](#)]
32. Dowling, A.P.; Williams, J.E.F. *Sound and Sources of Sound*; John Wiley & Sons, Inc.: New York, NY, USA, 1983; pp. 89–92.
33. Schuermans, B. Thermoacoustic modeling of a gas turbine using transfer functions measured under full engine pressure. *J. Eng. Gas Turbines Power* **2010**, *132*, 111503. [[CrossRef](#)]
34. Noiray, N.; Durox, D.; Schuller, T.; Candel, S. A unified framework for nonlinear combustion instability analysis based on the flame describing function. *J. Fluid Mech.* **2008**, *615*, 139–167. [[CrossRef](#)]
35. Palies, P.; Durox, D.; Schuller, T.; Candel, S. The combined dynamics of swirler and turbulent premixed swirling flames. *Combust. Flame* **2010**, *157*, 1698–1717. [[CrossRef](#)]

-
36. Palies, P.; Durox, D.; Schuller, T.; Candel, S. Nonlinear combustion instability analysis based on the flame describing function applied to turbulent premixed swirling flames. *Combust. Flame* **2011**, *158*, 1980–1991. [[CrossRef](#)]
 37. Munjal, M.L. *Acoustics of Ducts and Mufflers*, 2nd ed.; John Wiley & Sons Ltd: Chichester, UK, 2014; pp. 323–330.

Disclaimer/Publisher’s Note: The statements, opinions and data contained in all publications are solely those of the individual author(s) and contributor(s) and not of MDPI and/or the editor(s). MDPI and/or the editor(s) disclaim responsibility for any injury to people or property resulting from any ideas, methods, instructions or products referred to in the content.